Key Points:
- Net interannual radiative feedback is a weighted average of distinct feedbacks associated with distinct modes of variability
- Feedbacks obtained from interannual variability are distinct from those governing the response to CO_2 forcing
- Temperature-independent wind-driven air-sea fluxes are a critical forcing for subannual temperature variability

Supporting Information:
- Supporting Information S1

Correspondence to:
C. Proistosescu,
cproist@uw.edu

Radiative Feedbacks From Stochastic Variability in Surface Temperature and Radiative Imbalance

Cristian Proistosescu[1] [iD], **Aaron Donohoe[2]** [iD], **Kyle C. Armour[3,4]** [iD], **Gerard H. Roe[5]** [iD], **Malte F. Stuecker[4,6]** [iD], and **Cecilia M. Bitz[4]** [iD]

[1]Joint Institute for the Study of the Atmosphere and the Ocean, University of Washington, Seattle, WA, USA, [2]Applied Physics Laboratory, University of Washington, Seattle, WA, USA, [3]School of Oceanography, University of Washington, Seattle, WA, USA, [4]Department of Atmospheric Sciences, University of Washington, Seattle, WA, USA, [5]Department of Earth and Space Sciences, University of Washington, Seattle, WA, USA, [6]Cooperative Programs for the Advancement of Earth System Science, University Corporation for Atmospheric Research, Boulder, CO, USA

Abstract Estimates of radiative feedbacks obtained by regressing fluctuations in top-of-atmosphere (TOA) energy imbalance and surface temperature depend critically on the sampling interval and on assumptions about the nature of the stochastic forcing driving internal variability. Here we develop an energy balance framework that allows us to model the different impacts of stochastic atmospheric and oceanic forcing on feedback estimates. The contribution of different forcing components is parsed based on their impacts on the covariance structure of near-surface air temperature and TOA energy fluxes, and the framework is validated in a hierarchy of climate model simulations that span a range of oceanic configurations and reproduce the key features seen in observations. We find that at least three distinct forcing sources, feedbacks, and time scales are needed to explain the full covariance structure. Atmospheric and oceanic forcings drive modes of variability with distinct relationships between temperature and TOA radiation, leading to an effect akin to regression dilution. The net regression-based feedback estimate is found to be a weighted average of the distinct feedbacks associated with each mode. Moreover, the estimated feedback depends on whether surface temperature and TOA energy fluxes are sampled at monthly or annual time scales. The results suggest that regression-based feedback estimates reflect contributions from a combination of stochastic forcings and should not be interpreted as providing an estimate of the radiative feedback governing the climate response to greenhouse gas forcing.

Plain Language Summary Climate sensitivity quantifies the long-term warming the Earth will experience in response to the additional energy trapped in the system due to greenhouse gases. The physical processes that ultimately determine climate sensitivity — termed climate feedbacks — have been extensively investigated using information from natural variability in Earth's temperature and net energy imbalance. However, a complete physical model for what controls this natural variability has been lacking. We derive such a physical model and calibrate it to a hierarchy of numerical climate simulations of increasing complexity. We are able to answer several outstanding questions about previous estimates of climate feedbacks and sensitivity drawn from natural variability, such as what is the source of this variability, and how the estimates depend on the how the data is analyzed. We find that at least three different mechanisms for natural variability are needed to explain the relationship between temperature and energy imbalance and that none provide direct estimates of climate sensitivity .

1. Introduction

Joint observations of the Earth's temperature and energy imbalance allow for a unique opportunity to empirically constrain radiative feedbacks. However, the satellite record of Earth's top-of-atmosphere (TOA) radiative imbalance is relatively short and prone to calibration and drift errors, thus making estimates of the net imbalance less reliable than estimates of the relatively large stochastic fluctuations (Stevens & Schwartz, 2012). Consequently, significant effort has gone into estimating radiative feedbacks by regressing unforced fluctuations in global-mean TOA radiative imbalance against fluctuations in global-mean near-surface air temperature. The forced component of climate change is either assumed small or removed, and estimates of feedbacks associated with natural variability are often interpreted as either providing a direct estimate
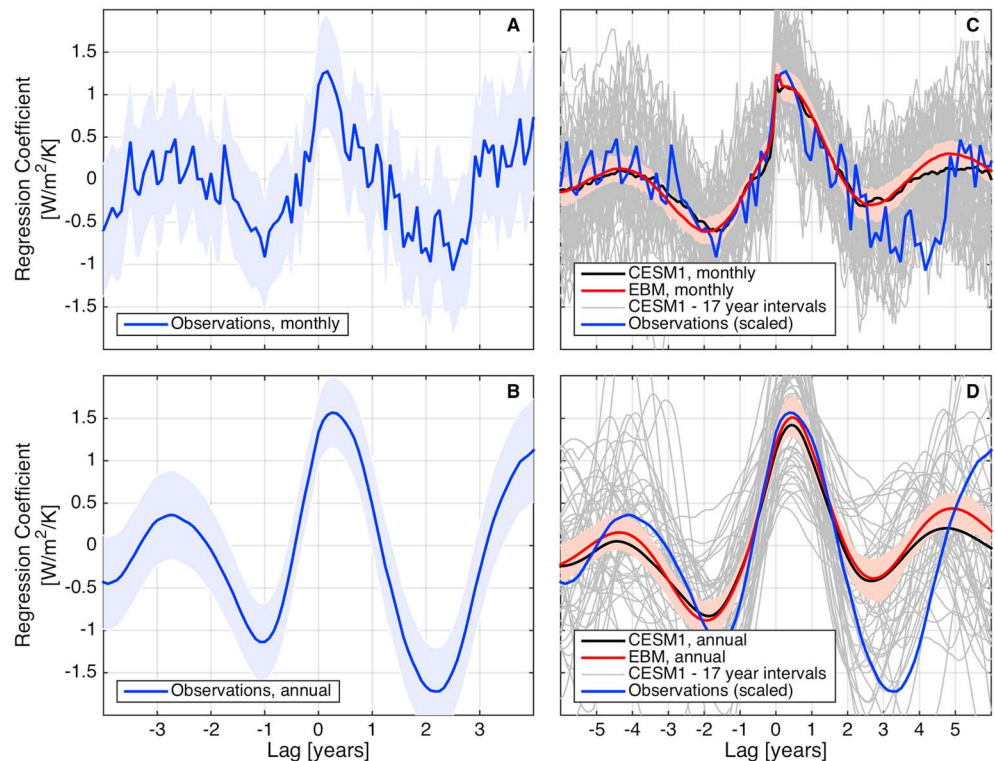
Figure 1. Lagged regressions between deseasonalized anomalies in global top-of-atmosphere radiation and surface temperature. (a) Observational data sets from March 2000 to October 2017. Monthly top-of-atmosphere radiation from Clouds and the Earth's Radiant Energy System Energy Balanced And Filled product (CERES EBAF). (Loeb et al., 2009; Wielicki et al., 1996) and monthly global mean surface temperature from Goddard Institute for Space Studies Surface Temperature Analysis (GISTEMP) (Hansen et al., 2010). Greenhouse gas and aerosol forcing is removed, and data are processed as in Donohoe et al. (2014). Shading illustrates 95% regression uncertainty estimates. (b) Same as (a) but for annually averaged anomalies. (c) Monthly anomalies from a 1,000-year-long preindustrial control run of CESM1 (black), and the EBM (red) prediction. Pink shading illustrates a 95% uncertainty estimates on EBM regression coefficient based on 1,000 Monte Carlo draws. Gray lines indicate lagged-regression structures from 50 nonoverlapping segments of the CESM1 simulation, each of equal length to the observational data set. Blue line indicates the observational lagged-regression structure, scaled as $r_{obs}^{scaled}(lag) = r_{obs}(lag \cdot 5/3)$, with the ratio of 5/3 mimicking the ratio of El Niño–Southern Oscillation periodicity in CESM1 and observations. (d) Same as (c) but for annually averaged anomalies. CESM1 = Community Earth System Model version 1; EBM = energy balance model.

of climate sensitivity to greenhouse gases (e.g., Chung et al., 2010; Dessler, 2010; Donohoe et al., 2014; Forster, 2016; Forster & Gregory, 2006; Trenberth et al., 2015; Tsushima & Manabe, 2013; Zhou et al., 2014) or used as an emergent constraint on long-term climate response (e.g., Zhou et al., 2015). For both direct estimates and emergent constraints, the interpretation of feedbacks associated with natural variability, and their applicability to long-term climate change, rests fundamentally on our ability to model the rich structure in the covariability of temperature and radiative anomalies (Klein & Hall, 2015), that is present in both models and observations (Forster, 2016, and Figure 1). However, this ability has yet to be demonstrated.

Several other issues with regression-based feedback estimates have been identified. Regression estimates rely on an often unstated assumption that variability in TOA radiation arises primarily as a response to variability in surface temperature which is, in turn, driven by nonradiative processes. Spencer and Braswell (2010, 2011) noted that if unforced TOA radiation itself plays an important role in driving surface temperature variability, then regression-based feedback estimates will be biased toward higher sensitivity—although the importance of unforced radiation anomalies has been challenged on methodological grounds (Murphy & Forster, 2010), and on the basis that air-sea heat flux variability, particularly associated with the El Niño–Southern Oscillation (ENSO), appears to be large relative to radiative variability (Dessler, 2011). Additionally, the net regression-based estimate of feedbacks associated with internal variability depends on the lag at which the regression is performed, and on whether monthly or annual data are used (Forster, 2016).

Here we use a stochastic energy balance framework to build an analytically tractable forward model that reproduces the full structure of the coupling between stochastic anomalies in global mean surface temperature anomalies and net TOA radiative imbalance. One approach to disentangling the drivers of interannual variability is to recognize that atmospheric and oceanic processes should operate at different characteristic time scales, and, perhaps, with different radiative impacts. We model the spectrum, phase, and covariance relationships of both temperature and radiation as seen in a hierarchy of general circulation model (GCM) simulations spanning a range of oceanic configurations. This allows us to parse the relative contribution of different stochastic atmospheric and oceanic forcing components and to interpret the value of the regression-based feedback as a function of the feedbacks elicited by different types of forcing on different time scales.

2. Energy Balance Framework

The classical building blocks for understanding climate variability are simple stochastically forced linear systems. The one-dimensional version is usually called a *Hasselmann* model (Hasselmann, 1976) and has the form

$$C\frac{dT}{dt} = -\lambda T + F,$$ (1)

where T here denotes global mean near-surface air temperature, C denotes heat capacity, λ denotes the radiative feedback, and F denotes stochastic forcing. Under a standard assumption of uncorrelated (white noise) forcing, the spectrum of temperature has the familiar Lorentzian shape transitioning from red noise at high frequencies to white noise at low frequencies (Figures 2a and 2b).

The form of the associated equation for TOA radiation depends upon the nature of the forcing (Dessler, 2011; Forster & Gregory, 2006; Spencer & Braswell, 2010, 2011). We first consider the case when forcing, F_1, is due to oceanic heat fluxes. The resulting TOA radiation, Q_1, then depends only on the radiative response to temperature change, T_1, according to

$$Q_1 = -\lambda T_1.$$ (2)

If, on the other hand, the system is forced only by stochastic TOA radiative anomalies, such as from cloud variability uncorrelated to T_1, then the forcing, F_2, will directly imprint upon TOA radiation:

$$Q_2 = -\lambda T_2 + F_2 = C\frac{dT_2}{dt}.$$ (3)

The two scenarios — oceanic and radiative forcing — can be distinguished through the phase relationships they induce between T and Q. Oceanic forcing leads to direct proportionality between T_1 and Q_1, and thus no phase lag (Figure 2b). Consequently, the lagged regression between T_1 and Q_1 is symmetric and equal to λ at lag zero (Figure 2c). Radiative forcing, however, causes TOA fluxes to be proportional to the rate of change of temperature, leading to a 90° phase lag (Figure 2e). The lagged regression then exhibits an antisymmetric structure with a discontinuity at zero lag (Figure 2f).

The third case we consider is that of an ENSO-type process, wherein the associated variability will be quasi-oscillatory, with a peak in the spectrum of the associated temperature variability. Such quasi-oscillatory behavior can be modeled either as a nonlinear oscillator (e.g., Battisti & Hirst, 1989) or as a stochastically forced linear oscillator (Thompson & Battisti, 2000). For analytical tractability we use the latter to model temperature ENSO-related temperature variability (Figure 2g). As ENSO variability is dominated by reorganization of oceanic heat content (Jin, 1997; Wyrtki, 1985), TOA radiation will be directly proportional to temperature, although we need to account for a possible lag between the peak in temperature and the peak in outgoing TOA radiation (Johnson & Birnbaum, 2017; Xie et al., 2016),

$$Q_3(t) = -\lambda T_3(t - \theta).$$ (4)

The lagged regression of temperature and TOA anomalies associated with ENSO variability is a shifted (by lag θ), decaying, quasi-oscillatory function (Figure 2i). Similar analyses of the lagged-regression symmetry have been used to disentangle forcing versus response relations in analyses of midlatitude sea-surface temperature (SST) variability (e.g., Bishop et al., 2017; Frankignoul, 1985; von Storch, 2000).
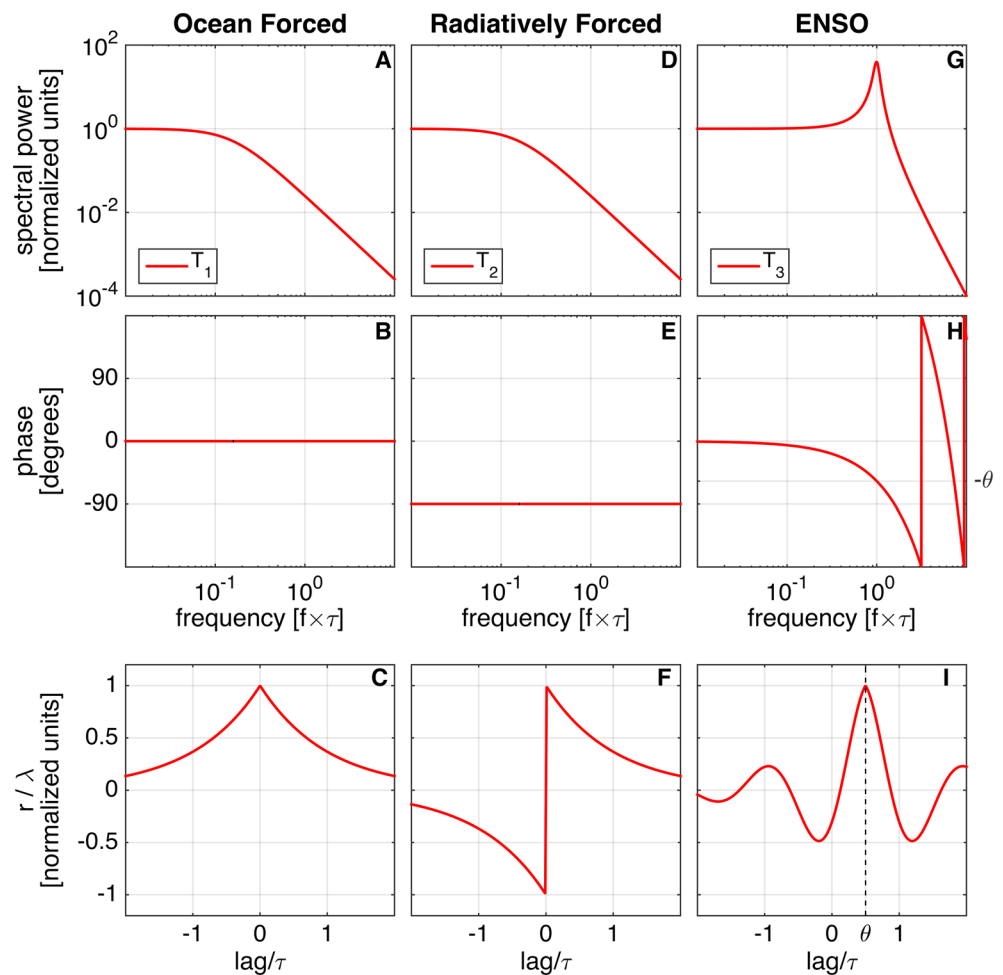
Figure 2. Spectrum, phase difference, and lagged regression of net top-of-atmosphere anomalies, *Q*, versus global-mean temperature, *T* for the idealized cases presented in section 2. (a)–(c) depicts the case of a Hasselmann-like model forced by uncorrelated (white noise) oceanic heat fluxes (equation (2)); (d)–(f) depicts a similar Hasselmann-like model but forced by top-of-atmosphere radiative anomalies (equation (3)); (g)–(i) depicts an El Niño–Southern Oscillation (ENSO)-like quasi-oscillatory process forced by exchanges between the surface and deep ocean (equation (4)).

Key to distinguishing each type of forcing is their distinct lagged-regression structures (Figures 2c, 2f, and 2i). When all three processes are operating at once, as in the coupled climate system, the net regression-based feedback will be a complex blend of the covariances structure associated with each forcing. We thus turn to GCM simulations to quantify the relative importance of each forcing type, to determine whether they may elicit distinct radiative feedbacks (Hansen et al., 2005; Winton et al., 2010), and to interpret the net feedback obtained by regression.

3. Model Hierarchy

The hierarchy of GCM simulations we employ consists of a set of preindustrial control simulations of the Community Earth System Model version 1 (CESM1), at 1° horizontal resolution, for which long integrations were made available within the Large Ensemble project (Kay et al., 2015). In order to quantify the roles of the various atmospheric and oceanic forcings in the regression between temperature and TOA radiation, simulations with three distinct types of model configuration are used: a coupled simulation with full ocean dynamics (OCN), a slab ocean simulation (SOM) using the spatially variable climatological mixed layer depth from the coupled simulation, and a fixed SST (fSST) simulation using the climatological SST and sea ice fields from the coupled simulation. The simulations are performed with a repeating seasonal cycle of insolation and a constant atmospheric composition representative of conditions in the year 1850. To ensure commensurate sampling uncertainties, we subset all simulations to a thousand years, equal to the length of the shortest

available simulation (SOM). All data are deseasonalized by removing the annual cycle frequency and its first three harmonics.

The fully coupled control simulation of CESM1 reproduces all salient features of the lagged regression structure in the observations (Figure 1): the relative magnitude of the regression coefficients over a range of lags using monthly data; the amplification of the zero-lag regression feedback when using annual data; the quasi-sinusoidal structure, the offset of the maximum covariance toward positive lags, and the sharp jump in regression coefficient around zero. As we will show, the discrepancy in the periodicity of the sinusoidal structure in the lagged regression is attributable to the longer periodicity of CESM1's ENSO cycle compared to the observations. This discrepancy be accounted for by rescaling the observed lagged regression by the ratio of model ENSO period to observed ENSO period (Figures 1c and 1f). In what follows, we build and tune an energy balance model (EBM) to replicate the regression statistics of each simulation in the CESM1 hierarchy in order to interpret the behavior of the coupled climate system.

3.1. fSST Simulation

The spectrum of near-surface air temperature in the fSST simulation (Figure 3a) has the expected Lorentzian profile, flat at low frequencies and damped at high frequencies. The phase relation between T and Q is centered on zero (Figure 3b), indicating that the dominant forcing on the atmosphere is provided by heat fluxes from the ocean, rather than from TOA radiative variability. Traditionally, the oceanic source of variance is assumed to be associated with ENSO (Dessler, 2010, 2011, 2013; Murphy & Forster, 2010; Trenberth et al., 2011, 2015). However, the fSST simulation does not contain ocean-dynamics or ENSO-like SST variability; the source of near-surface air temperature variability is instead provided by stochastic turbulent atmosphere-ocean fluxes.

We thus build on previous two layer models of atmosphere-ocean exchanges (Barsugli & Battisti, 1998; Cronin & Emanuel, 2013) and consider an atmosphere, with temperature T_a and heat capacity C_a, coupled to a surface ocean mixed layer, with temperature T_o and heat capacity C_o. Due to its small heat capacity, the land is assumed to be in equilibrium with the atmosphere on monthly time scales. Heat fluxes at the air-sea interface depend on wind speed and on atmosphere-ocean gradients in temperature and humidity. For small perturbations around a steady state, humidity anomalies can be linearized and approximated as proportional to temperature anomalies. The net atmosphere-ocean fluxes can thus be approximated as $\mathcal{H} \propto U(T_a - T_o)$ (e.g., Hartmann, 2015). Ignoring second order terms, anomalous air-sea fluxes can be decomposed to yield two terms: (i) a damping term, $\lambda_{ao}(T_a - T_o) \propto \bar{U}(T'_a - T'_o)$, proportional to the climatological time-mean wind speed, $\bar{U}$, and temperature gradient anomalies $(T'_a - T'_o)$; and (ii) a stochastic forcing term $F_{ao} \propto U'\overline{(T_a - T_o)}$, proportional to surface wind anomalies with a white-noise spectrum (Figure S1 in the supporting information), and the time-mean temperature gradient. For the remainder of the text we will drop the apostrophe notation, such that all values are taken to represent anomalies from steady state. The turbulent feedback λ_{ao} is typically an order of magnitude larger than the radiative feedbacks term, denoted $\lambda_{rad,a}T_a$ and $\lambda_{rad,o}T_o$ (Barsugli & Battisti, 1998; Cronin & Emanuel, 2013). The inclusion of a $\lambda_{rad,o}$ term accounts for the fact that land-atmosphere variability and mixed-layer variability exhibit different temperature patterns and may therefore excite different radiative feedbacks (Andrews & Webb, 2018; Andrews et al., 2015; Armour et al., 2013; Proistosescu & Huybers, 2017; Rose et al., 2014). $\lambda_{rad,o}$ also accounts for radiation emitted by the surface ocean that is not absorbed by the atmosphere. Finally, we consider stochastic radiative anomalies uncorrelated with surface temperature over both land and ocean, $F_{rad} = F_{rad,l} + F_{rad,o}$, and write the full model as

$$C_a \frac{dT_a}{dt} = -\lambda_{rad,a}T_a - \lambda_{ao}(T_a - T_o) + F_{ao} + F_{rad,l} \tag{5}$$

$$C_o \frac{dT_o}{dt} = -\lambda_{rad,o}T_o + \lambda_{ao}(T_a - T_o) - F_{ao} + F_{rad,o}, \tag{6}$$

$$Q = -\lambda_{rad,a}T_a - \lambda_{rad,o}T_o + F_{rad}. \tag{7}$$

In the fSST configuration we disregard equation (6), while in equation (5) T_o is kept equal to 0. Additionally, the zero phase lag (Figure 3b) indicating predominant oceanic forcing means that $F_{ao} \gg F_{rad,l}$. This is supported by the fact that the spectrum of TOA fluxes in the CESM1 fSST simulation is 2 orders of magnitude smaller than that of surface heat fluxes at frequencies $f \gg \lambda_{ao}/C_a \gg \lambda_{rad,a}/C_a$, where the forcing terms dominate the feedback terms in equation (5), (Figure S2 in the supporting information). Denoting $C_1 = C_a\lambda_{rad,a}(\lambda_{rad,a} + \lambda_{ao})^{-1}$, $F_1 = F_{ao}\lambda_{rad,a}(\lambda_{rad,a} + \lambda_{ao})^{-1}$, $\lambda_1 = \lambda_{rad,a}$, and after some reorganization, we can now write a Hasselmann
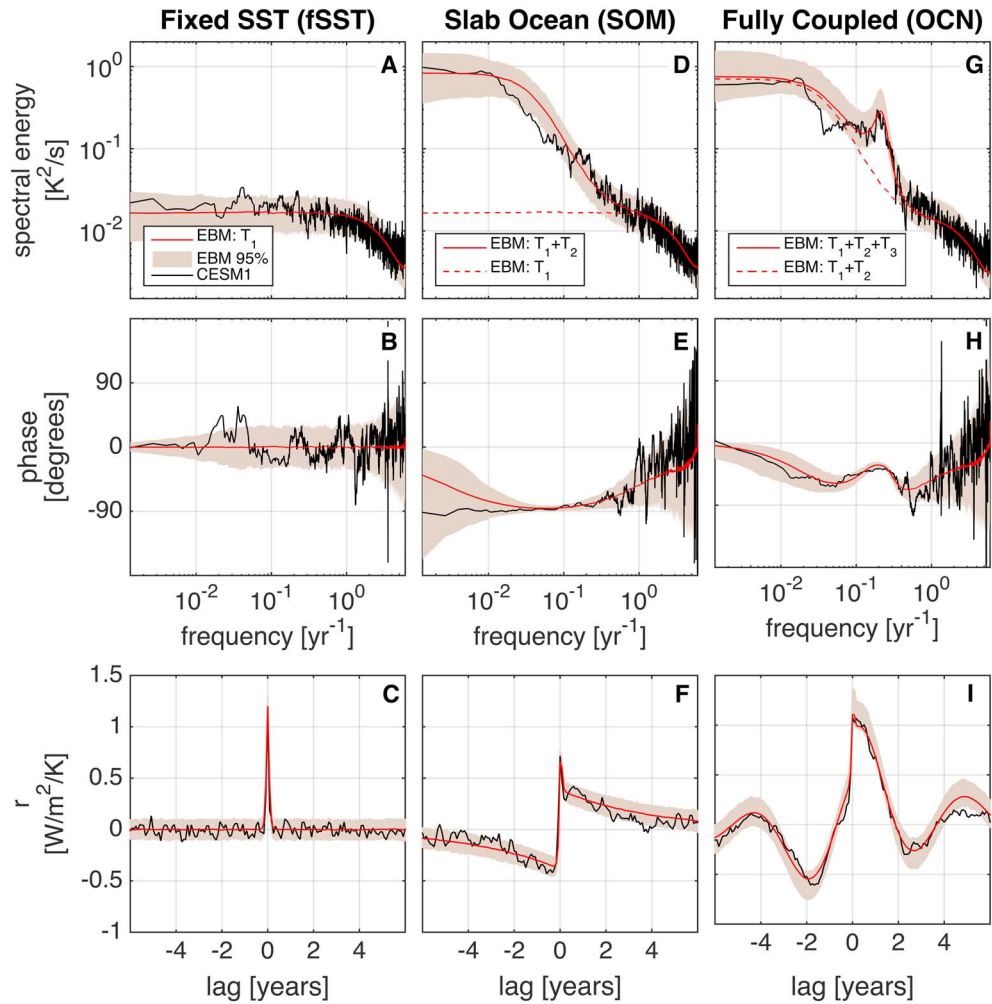
AGU
100
ADVANCING EARTH
AND SPACE SCIENCE

Geophysical Research Letters

10.1029/2018GL077678

Figure 3. Analytical spectrum, phase difference, and lagged regression coefficient, *r*, of net top-of-atmosphere anomalies, *Q*, versus global mean near-surface air temperature, *T* in a CESM1 control run hierarchy. The hierarchy consists of a fixed SST run (a–c), a slab ocean run (d–f), as well as the fully coupled control run (g–i). The statistics are depicted for CESM1 integrations (black), along with EBM (red) fit. A 95% range of EBM realizations is depicted, based on 1,000 Monte Carlo draws. Spectra are computed using a Multitaper algorithm with eight windows. SST = sea surface temperature ; CESM1 = Community Earth System Model version 1; EBM = energy balance model; OCN = ocean dynamics.

model akin to equations (1) and (2), for the atmospheric temperature, $T_1 = T_a$, in the fSST simulation:

$$C_1 \frac{dT_1}{dt} = -\lambda_1 T_1 + F_1, \tag{8}$$

$$Q_1 = -\lambda_1 T_1 + F_{rad}, \tag{9}$$

with $\tau_1 = C_1/\lambda_1 = 0.05$ years, and $\lambda_1 = 1.2 \, \text{W} \cdot \text{m}^{-2} \cdot \text{K}^{-1}$, as fit to the fSST simulation (Appendix A) and consistent with those derived from first-order principles by Cronin and Emanuel (2013).

Since T_1 is forced by atmosphere-ocean fluxes, the radiative term is not correlated with temperature, and its presence in equation (9) introduces uncertainty in the phase relation (Figure 3b) without altering the zero mean. The predicted lagged regression matches the fSST simulation (Figure 3c) and is consistent with an oceanic source of variance (Figure 2c). Thus, air temperature variability driven by surface fluxes shows a lag-zero regression of $1.2 \, \text{W} \cdot \text{m}^{-2} \cdot \text{K}^{-1}$.

3.2. SOM Simulation

We next consider the SOM, in which the atmosphere is coupled to a mixed layer ocean with SSTs that are allowed to evolve thermodynamically, but without ocean dynamics. The spectrum of near-surface air temperature (Figure 3d) is consistent with the spectrum of the fSST simulation at high frequencies but displays

additional variability at frequencies lower than the atmospheric adjustment time scale. We model this additional variability associated with an active mixed layer by considering a second linear mode of variability, T_2, that is sufficient to capture the increase in variance on multiannual time scales.

The phase relation between TOA anomalies and temperature (Figure 3e) goes from zero at high frequencies, consistent with the fSST simulation, to 90° on interannual time scales where the second mode dominates the variability, indicating a radiative source of variance for T_2 (compare with Figure 2e). Indeed, since this mode arises on time scales longer than the equilibration time of the atmosphere ($\tau_1 = 0.05$ years), the atmosphere and ocean layer will be in equilibrium with one another. On these time scales, we can approximate $T_2 \approx T_a \approx T_o$ and sum equations (5) and (6) canceling the F_{ao} terms. This slower mode, T_2, then represents the evolution of the joint atmosphere-mixed layer primarily driven by radiative TOA perturbations. Denoting $C_2 = C_a + C_o$, $\lambda_2 = \lambda_{rad,a} + \lambda_{rad,o}$, $F_2 = F_{rad}$, the Hasselmann model for the second mode can be written akin to equations (1) and (3) as

$$C_2 \frac{dT_2}{dt} = -\lambda_2 T_2 + F_{rad},$$ (10)

$$Q_2 = -\lambda_2 T_2 + F_{rad},$$ (11)

with $\tau_2 = C_2/\lambda_2 = 2$ years and $\lambda_2 = 0.9\,\text{W} \cdot \text{m}^{-2} \cdot \text{K}$, as fit to the SOM simulation.

The full behavior of the SOM simulation is thus modeled as the sum of the responses of the surface flux-driven mode, T_1, and the radiative driven mode, T_2. These two modes, as described by equations (8)–(11), are a good approximation to the actual eigenmodes of the coupled system (equations (5) and (6)), since $\tau_2 \gg \tau_1$ and $\lambda_{ao} \gg \lambda_{rad}$ (Cronin & Emanuel, 2013). Both the phase and the lagged regression predicted by $T_1 + T_2$ match the SOM simulation (Figures 3e and 3f) and are consistent with a combination of ocean and radiatively forced modes (Figures 2a and 2e, and 2c and 2f). The lagged-regression structure shows both the narrow peak at zero lag associated with ocean-forced T_1 as well as a discontinuity at zero associated with a radiatively forced mode. Notably, the height of the zero-lag peak for the SOM simulation is lower than the height of the peak in the fSST simulation, where it is equal to λ_1.

3.3. Coupled Model With Full Ocean Dynamics

The fully coupled simulation includes the same physics described above but also permits coupled ocean-atmosphere dynamics that give rise to quasi-oscillatory interannual variability, primarily in the form of an ENSO mode of variability. This variability is identifiable by the narrowband concentration of power in the spectral peak centered on a frequency of $f_E = 1/4.5$ years (Figure 3g). Since an oscillatory solution in a linear model requires at least two eigenmodes, we model the additional ENSO variability as a stochastically forced damped harmonic oscillator (Thompson & Battisti, 2000, 2001). We further allow that the peak in TOA fluxes through an ENSO cycle lags surface temperatures (Johnson & Birnbaum, 2017; Xie et al., 2016), such that the response of the third mode becomes

$$\frac{1}{\omega_E^2} \frac{d^2 T_3}{dt^2} + \frac{2}{\tau_3 \omega_E^2} \frac{dT_3}{dt} + T_3 = \eta,$$ (12)

$$Q_3(t) = \lambda_3 \cdot T_3(t - \theta),$$ (13)

where η is a white noise stochastic driving force (Thompson & Battisti, 2001); $\omega_E = 2\pi f_E$ is the resonant angular frequency of the oscillator, $\tau_3 = 4$ years is a damping time that controls the width of the peak, $\theta = 8$ months is the lag of radiation relative to temperature, and $\lambda_3 = 3.0\,\text{W} \cdot \text{m}^{-2} \cdot \text{K}^{-1}$ is the radiative feedback associated with the ENSO-related temperature variability. The larger magnitude of λ_3 relative to λ_1, λ_2, can be understood in terms of the difference in the temperature patterns associated with each mode. Whereas land-atmosphere and mixed-layer variability in CESM1 is dominated by the high latitudes (Xie et al., 2016), ENSO variability is centered on the tropics and is therefore expected to lead to stronger radiative damping, and therefore a larger λ_3 (Rose et al., 2014; Winton et al., 2010).

Temperature and TOA variability in the fully coupled simulation (OCN) are modeled as $\sum T_j$, and $\sum Q_j$. Consistent with the CESM1 control simulation (Figure 3j), relative phase goes as $\phi = \omega\theta \approx 53°$ at the resonant frequency. The lagged-regression structure predicted by $\sum T_j$ and $\sum Q_j$ match the OCN simulation (Figure 3i) and is consistent with a combination of the three idealized modes (Figures 2b, 2e, and 2h, and 2c, 2f, and 2i) operating at once.

4. Regression Coefficients and Radiative Feedbacks

Having assembled a full conceptual model that reproduces the spectral characteristics of the GCM, we are now in a position to understand the full structure of the lagged regression (Figure 1), and why it depends on both lag and sampling interval. The lagged regression is equal to the superposition of the distinct feedbacks associated with each mode, weighted by each mode's relative temperature variance and its autocorrelation (see Appendix A for derivation):

$$r(\text{lag}) = \sum_j \lambda_j \left(\frac{\sigma_{T_j}^2}{\sigma_{T_{\text{total}}}^2} \right) \rho_j(\text{lag}), \tag{14}$$

where $\sigma_{T_j}^2 = \text{var}\left(T_j\right)$ is the total variance of mode T_j and $\rho_j(t)$ its autocorrelation function. The regression values at zero lag and at the ENSO lag θ can be well approximated as

$$r(0) = \lambda_1 \left(\frac{\sigma_{T_1}^2}{\sigma_{T_{\text{total}}}^2} \right) + \lambda_3 \left(\frac{\sigma_{T_3}^2}{\sigma_{T_{\text{total}}}^2} \right) \left[e^{-\theta/\tau_3} \cos\left(\omega_E \theta \right) \right], \tag{15}$$

$$r(\theta) \approx \lambda_2 \left(\frac{\sigma_{T_2}^2}{\sigma_{T_{\text{total}}}^2} \right) \left[e^{-\theta/\tau_2} \right] + \lambda_3 \left(\frac{\sigma_{T_3}^2}{\sigma_{T_{\text{total}}}^2} \right). \tag{16}$$

For CESM1, the standard deviations for monthly samples are $\sigma_{T_1} = 0.10, \sigma_{T_2} = 0.08, \sigma_{T_3} = 0.07$ K, the feedback parameters are $\lambda_1 = 1.2, \lambda_2 = 0.9, \lambda_3 = 3.0$ W $\cdot$ m^{-2} $\cdot$ K^{-1}, and net regression feedbacks are $r(0) = 1.2$ W $\cdot$ m^{-2} $\cdot$ K^{-1} and $r(\theta) = 1.0$ W $\cdot$ m^{-2} $\cdot$ K^{-1}. We repeat our analysis by performing integrations of the same model hierarchy within an earlier version of the GCM, the Community Climate System Model version 4 (CCSM4; Bitz et al., 2012; Gent et al., 2011). Within CCSM4, the variance is partitioned differently between the three modes, with ENSO now the dominant mode. Standard deviations are $\sigma_{T_1} = 0.10, \sigma_{T_2} = 0.08, \sigma_{T_3} = 0.13$ K, the feedback parameters are $\lambda_1 = 1.5, \lambda_2 = 1.5, \lambda_3 = 2.2$ W $\cdot$ m^{-2} $\cdot$ K^{-1}. The net regression feedbacks are $r(0) = 1.2, r(\theta) = 1.1$ W $\cdot$ m^{-2} $\cdot$ K^{-1}, nearly identical to CESM1, despite the significant differences in the feedbacks and relative variances of each mode.

Equations (14)–(16) provide insight into how and why net regression feedback estimates depend on both lag and sampling interval. At zero lag, the autocorrelation of the second, radiatively forced mode, $\rho_2(0)$ is 0, but T_2 still contributes to the total temperature variance. This presence of additional variance in the predictor variable T that is not manifested in the regressed variable Q is called regression dilution (Fuller, 2009) and biases the net feedback low relative to a scenario where all variability in T projects identically on Q. This would imply a bias toward higher sensitivity, if one were to naively interpret it as such. Furthermore, ENSO variability contributes fully to the temperature variance through $\sigma_{T_3}^2$, but its contribution to the covariance of T and Q at zero lag is damped due to the lag θ. The lagged regression at the ENSO lag θ suffers from similar issues. The first mode, forced by surface fluxes, contributes to the temperature variance, but not to the covariance, since $\theta \gg \tau_1$ and $\rho_1(\theta) \approx 0$, leading to regression dilution. The bias is enhanced by the fact that the contribution of T_2 is also damped by a factor of $e^{-\theta/\tau_2}$ (equation (16)).

The different correlation time scales τ_j of the different components mean that smoothing (from monthly to annual) does not affect all modes equally. Thus, the ratio of $\sigma_{T_j} / \sum \sigma_{T_k}$ is a function of sampling interval, leading to different net regression estimates from monthly and from annual data. Using annual averages most strongly suppresses the first mode of variability, such that in CESM1 σ_{T_1} drops from 0.10 to 0.02 K on annual time scales, while σ_{T_2} changes only slightly from 0.09 to 0.08 K, as does σ_{T_3} from 0.08 to 0.07 K. Thus, the regression dilution effect of the surface flux forced mode is greatly reduced with annual sampling, leading to a larger value of the regression coefficient, as observed by Forster (2016) and seen in Figure 1.

5. Discussion

We find that natural variability in temperature and radiative anomalies is not dominated by a single source of forcing. Rather, variability arises in response to different forcing components exciting different radiative responses. Our results highlight the critical importance of high-frequency variability associated with wind-forced air-sea fluxes. Consistent with previous studies suggesting a dominant ocean source for the forcing (Dessler, 2011; Murphy & Forster, 2010), 70% and 81% of the near-surface air temperature variance is attributable to ocean-forced modes T_1 and T_3 in CESM1 and CCSM4, respectively. However, this is the result

of two independent modes, with no single dominant mode, such that the regression-based estimate of the net feedback is an amalgamation of several mechanisms with different feedbacks, time scales, and lags.

In all likelihood other modes of variability may be present in the real climate system, such as centennial-scale variability associated with Southern Ocean variability (Martin et al., 2013) or modulation of ENSO variability (Wittenberg, 2009). Indeed, it seems fortuitous that variability in CESM1 and CCSM4 can be described using only three dominant modes. This could partially be attributable to the fact that outside of the ENSO band, coupled atmospheric-ocean dynamics in the OCN simulation do not excite significantly different decadal variability from the SOM simulation (Xie et al., 2016). However, it is possible that in other models—or in the real climate system—there may be significantly more multidecadal variability arising through coupled ocean-atmosphere mechanisms, such as the Pacific Decadal Oscillation or Atlantic Multidecadal variability. The framework developed here should be broadly applicable to any decomposition of variability into separate modes of variability.

Importantly, we find the regression-based estimate of the net feedback to be a poor analog for the equilibrium feedback in response to CO_2 forcing, even in a perfect model setup. For CESM1 the feedback in response to CO_2 forcing is $\lambda_{CO_2} = 0.9 \, \text{W} \cdot \text{m}^{-2} \cdot \text{K}^{-1}$ (Meehl et al., 2013), compared to $r(0) = 1.2$ and $r(\theta) = 1.1 \, \text{W} \cdot \text{m}^{-2} \cdot \text{K}^{-1}$. For CCSM4, $\lambda_{CO_2} = 1.25 \, \text{W} \cdot \text{m}^{-2} \cdot \text{K}^{-1}$ (Bitz et al., 2012), nearly 40% larger, despite regression-based estimates of interannual feedback of $r(0) = 1.2$ and $r(\theta) = 1.0 \, \text{W} \cdot \text{m}^{-2} \cdot \text{K}^{-1}$, nearly identical to CESM1. The nearly identical values of $\rho(0)$ and $\rho(\theta)$ in the two models arise through compensations in the values of variances and feedbacks of the individual modes. In particular, the ENSO mode, T_3 has the lowest relative variance in CESM1 (23%), and the highest relative variance in CCSM4 (53%), but the change in relative variance is compensated by the change in the radiative feedback magnitude of λ_3.

In lieu of a direct estimate from interannual variability, there is evidence that the ensemble spread in regression-based (e.g., Zhou et al., 2015) or fluctuation-dissipation-based (e.g., Cox et al., 2018) estimates of interannual feedbacks is strongly related to the ensemble spread in climate sensitivity across fully-coupled models. However, any emergent constraint using a bulk regression-based feedback as their basis should be treated with caution, as the intermodel spread is not simply a function of the radiative processes. The model ensemble spread will be strongly influenced by the significant ensemble spread of the variance and time scales associated with different modes of variability (e.g., Chen et al., 2017, for spread in ENSO variability). One possible path forward is identifying commonalities between the feedbacks associated with individual modes or time scales and the feedbacks governing long-term warming, such as has been recently done for the radiative feedback associated with the ENSO frequency (Lutsko & Takahashi, 2018).

However, constraining these modes in the observational record is expected to provide several challenges. A complicating factor in using observational data is that global-mean temperature measurements often consist of a blend of air temperature over land and SST over the ocean. This could lead to a subsampling of the fast mode. However, this bias could be quantified by using a blended model output that would mimic observational sampling (Richardson et al., 2016) or by only analyzing time scales longer than a year, where sea-surface and air temperature are expected to covary. Using a hierarchy of multicentury GCM simulations allowed us to constrain the model parameters to a high degree of accuracy. However, the large number of total EBM parameters and the relatively short observational record will result in trade-offs between likely parameter values that will need to be carefully quantified. Additionally, while this work highlights the importance of the temporal structure of the coupling between temperature and radiation, each of the modes of variability also has a particular spatial pattern that could prove useful in constraining it. Future work should focus on developing a statistical framework to fit the conceptual model to the short and noisy observational record and on making use of the spatial structure associated with each temporal mode.

Appendix A: Analytical Derivations and Model Fitting

Here we derive analytical solutions to the EBM fit to output from the three CESM1 experiments. For zero-mean processes, the lag-t regression of TOA anomalies relative to temperature anomalies is a ratio of the lagged cross covariance to the zero-lag temperature autocovariance,

$$r(t) = \frac{C_{QT}(t)}{C_{TT}(0)}, \tag{A1}$$

with the lag-t autocovariance and cross covariance, $C_{YX}(t) = \langle Y(t')X(t'+t) \rangle$, computed from the autospectra or cross spectra $S_{YX}(\omega) = \langle Y(\omega)X^*(\omega) \rangle$, using the Wiener-Khinchin theorem as

$$C_{XY}(t) = \int_{-\infty}^{\infty} S_{XY}(\omega)e^{-i\omega t}\mathrm{d}\omega. \tag{A2}$$

Thus, we need to compute the spectrum of temperature, S_{TT} and the cross spectrum of TOA anomalies and temperature, S_{QT}. The phase lag is computed as the phase of the complex cross spectrum.

A1. Fixed Sea Surface Temperatures

Taking the Fourier transform of equations (8) and (9) and denoting $\tau_1 = C_1/\lambda_1$, $\sigma_{F_1} = \langle F_1 F_1^* \rangle (\omega)$, and $\sigma_{T_1} = C_{T_1 T_1}(0)$,

$$i\omega\tau_1\lambda_1 T_1 = -\lambda_1 T_1 + F_1 \tag{A3}$$

$$Q_1 = -\lambda_1 T_1 + F_{\mathrm{rad}} \tag{A4}$$

$$S_{T_1 T_1} = \frac{\sigma_{F_1}^2}{\lambda_1^2}\frac{1}{1+\omega\tau_1^2} \tag{A5}$$

$$S_{Q_1 T_1} = \frac{\sigma_{F_1}^2}{\lambda_1}\frac{1}{1+\omega\tau_1^2} + \frac{1}{\lambda_1}\frac{\langle F_1 \cdot F_{\mathrm{rad}}^* \rangle}{1+i\omega\tau_1} \tag{A6}$$

Using the assumption that $\langle F_1 F_{\mathrm{rad}}^* \rangle = 0$,

$$C_{T_1 T_1}(0) = \frac{\sigma_{F_1}^2}{\lambda_1^2}\int_{-\infty}^{\infty}\frac{e^{-i\omega t}}{1+\omega^2\tau_1^2}\mathrm{d}\omega\bigg|_{t=0} = \frac{\sigma_{F_1}^2}{2\lambda_1^2\tau_1} = \sigma_{T_1}^2 \tag{A7}$$

$$C_{Q_1 T_1}(t) = \frac{\sigma_{F_1}^2}{\lambda_1}\int_{-\infty}^{\infty}\frac{e^{-i\omega t}}{1+\omega^2\tau_2^2}\mathrm{d}\omega = \frac{\sigma_{F_1}^2}{2\lambda_1\tau_1}e^{-|t|/\tau_1} \tag{A8}$$

$$C_{Q_1 T_1}(t) = \lambda_1\sigma_{T_1}e^{-|t|/\tau_1} \tag{A9}$$

$$r^{(\mathrm{fSST})} = \lambda_1 e^{-|t|/\tau_1} \tag{A10}$$

A2. Slab Ocean Model

Taking the Fourier transform of equations (10) and (11) and denoting $\tau_2 = C_2/\lambda_2$, $\sigma_{F_2} = \langle F_2 F_2^* \rangle (\omega)$, and $\sigma_{T_2} = C_{T_2 T_2}(0)$,

$$i\omega\tau_2\lambda_2 T_2 = -\lambda_2 T_2 + F_2 \tag{A11}$$

$$Q_2 = -\lambda_2 T_2 + F_2 = i\omega\tau_2\lambda_2 T_2 \tag{A12}$$

$$S_{T_2 T_2} = \frac{\sigma_{F_2}^2}{\lambda_2^2}\frac{1}{1+\omega^2\tau_2^2} \tag{A13}$$

$$S_{Q_2 T_2} = \frac{\sigma_{F_2}^2}{\lambda_2}\frac{i\omega\tau_2}{1+\omega^2\tau_2^2} \tag{A14}$$

$$C_{T_2 T_2}(0) = \frac{\sigma_{F_2}^2}{\lambda_2^2}\int_{-\infty}^{\infty}\frac{e^{-i\omega t}}{1+\omega^2\tau_2^2}\mathrm{d}\omega\bigg|_{t=0} = \frac{\sigma_{F_2}^2}{2\lambda_2^2\tau_2} = \sigma_{T_2}^2 \tag{A15}$$

$$C_{Q_2 T_2}(t) = \frac{\sigma_{F_2}^2}{\lambda_2} \int_{-\infty}^{\infty} \frac{i\omega e^{-i\omega t}}{1 + \omega^2 \tau_2^2} \, d\omega = \frac{\sigma_{F_2}^2}{2\lambda_2 \tau_2} e^{-|t|/\tau_2} \operatorname{sign}(t) \tag{A16}$$

$$C_{Q_2 T_2}(t) = \lambda_2 \sigma_{T_2} e^{-|t|/\tau_2} \operatorname{sign}(t) \tag{A17}$$

Since the modes are assumed independent,

$$S_{TT}^{(\text{SOM})} = S_{T_1 T_1} + S_{T_2 T_2} \tag{A18}$$

$$S_{QT}^{(\text{SOM})} = S_{Q_1 T_1} + S_{Q_2 T_2} \tag{A19}$$

$$C_{TQ}^{(\text{SOM})} = C_{Q_1 T_1} + C_{Q_2 T_2} \tag{A20}$$

$$C_{TT}^{(\text{SOM})} = \sigma_{T_1} + \sigma_{T_2} \tag{A21}$$

$$r^{(\text{SOM})}(t) = \lambda_1 \left(\frac{\sigma_{T_1}^2}{\sigma_{\text{total}}^2} \right) \left(e^{-|t|/\tau_1} \right) + \lambda_2 \left(\frac{\sigma_{T_2}^2}{\sigma_{\text{total}}^2} \right) \left(e^{-|t|/\tau_2} \operatorname{sign}(t) \right) \tag{A22}$$

A3. Coupled Run With Full Ocean Dynamics
Taking the Fourier transform of equations (12) and (13) and denoting $\omega_E^* = \omega_E - 1/\tau_3$, $\sigma_\eta^2 = \langle \eta \eta^* \rangle$

$$-\frac{\omega^2}{\omega_E^2} T_3 + \frac{2i\omega}{\tau_3 \omega_E^2} T_3 + T_3 = \eta \tag{A23}$$

$$Q_3 = \lambda_3 T_3 e^{i\omega\theta} \tag{A24}$$

$$S_{T_3 T_3} = \frac{\sigma_\eta^2}{\left(\omega_E^2 - \omega^2 \right)^2 + 4\omega^2 \tau_3^{-2}} \tag{A25}$$

$$S_{Q_3 T_3} = \frac{\lambda_3 \sigma_\eta^2 e^{i\omega\theta}}{\left(\omega_E^2 - \omega^2 \right)^2 + 4\omega^2 \tau_3^{-2}} \tag{A26}$$

The autocovariance and cross covariance are (Wang & Uhlenbeck, 1945):

$$C_{T_3 T_3}(0) = \sigma_\eta^2 \omega_E^2 \int_{-\infty}^{\infty} \frac{e^{-i\omega t}}{\left(\omega_E^2 - \omega^2 \right)^2 + 4\omega^2 \tau_3^{-2}} \, d\omega \Bigg|_{t=0} \tag{A27}$$

$$C_{T_3 T_3}(0) = \pi \sigma_\eta^2 \omega_E^2 \tag{A28}$$

$$C_{Q_3 T_3}(t) = \lambda_3 \sigma_\eta^2 \omega_E^2 \int_{-\infty}^{\infty} \frac{e^{-i\omega(t-\theta)}}{\left(\omega_E^2 - \omega^2 \right)^2 + 4\omega^2 \tau_3^{-2}} \, d\omega \tag{A29}$$

$$C_{Q_3 T_3}(t) = \lambda_3 \pi \sigma_\eta^2 \omega_E^2 e^{-|t-\theta|/\tau_3} \left[\cos\left(\omega_E^*(t-\theta) \right) + \frac{1}{\omega_E^* \tau_3} \sin\left(\omega_E^*(t-\theta) \right) \right] \tag{A30}$$

Using the independence of the modes,

$$S_{TT}^{(OCN)} = \sum_{j=1}^{3} S_{T_j T_j} \tag{A31}$$

$$C_{QT}^{(OCN)} = \sum_{j=1}^{3} C_{Q_j T_j} \tag{A32}$$

$$r(t) = \sum_{j=}^{3} \lambda_j \frac{\sigma_{T_j}^2}{\sigma_{T_{total}}^2} \rho_j(t) \tag{A33}$$

$$\rho_1(t) = e^{-|t|/\tau_1} \tag{A34}$$

$$\rho_2(t) = e^{-|t|/\tau_2} \text{sign}(t) \tag{A35}$$

$$\rho_3(t) = e^{-|t-\theta|/\tau_3} \left[\cos\left(\omega_E^*(t-\theta)\right) + \frac{1}{\omega_E^* \tau_3} \sin\left(\omega_E^*(t-\theta)\right) \right] \tag{A36}$$

At $t = 0$, $\rho_2(0) = 0$. Since $\theta \approx 8$ months, and $\omega_E = 2\pi/5$ rad/years, $\rho_3(0)$ will be dominated by the cosine term.

$$\rho_3(0) \approx e^{-\theta/\tau_3} \cos\left(\omega_E^* \theta\right) \tag{A37}$$

At $t = \theta$ it follows from $\tau_1 \ll \theta$ that $\rho_1(\theta) \approx 0$.

A4. Fitting Procedure

Parameters are obtained in the following manner and order. $(\sigma_{F_1}^2 \lambda_1^{-2})$ and τ_1 are obtained by a nonlinear least squares (NLSQ) of equation (A5) to the periodogram of near-surface air temperature from the fSST simulation (Figure 3a). λ_1 is obtained using an NLSQ of equation (A10) to the lagged regression of TOA versus near-surface air temperature in the fSST simulation (Figure 3c). $(\sigma_{F_2}^2 \lambda_{-2})$ and τ_2 are obtained by NLSQ of equation (A18) to the periodogram of near-surface air temperature in the SOM simulation (Figure 3d). λ_2 is obtained using an NLSQ of equation (A22) to the lagged regression of TOA versus near-surface air temperature in the fSST simulation (Figure 3f). σ_η^2, ω_E, and τ_3 are obtained by NLSQ of equation (A31) to the periodogram of near-surface air temperature in the OCN simulation (Figure 3d). λ_3 and θ are obtained using an NLSQ of equation (A33) to the lagged regression of TOA versus near-surface air temperature in the OCN simulation.

References

Andrews, T., Gregory, J. M., & Webb, M. J. (2015). The dependence of radiative forcing and feedback on evolving patterns of surface temperature change in climate models. *Journal of Climate*, *28*(4), 1630–1648.

Andrews, T., & Webb, M. J. (2018). The dependence of global cloud and lapse rate feedbacks on the spatial structure of tropical Pacific warming. *Journal of Climate*, *31*(2), 641–654.

Armour, K. C., Bitz, C. M., & Roe, G. H. (2013). Time-varying climate sensitivity from regional feedbacks. *Journal of Climate*, *26*(13), 4518–4534.

Barsugli, J. J., & Battisti, D. S. (1998). The basic effects of atmosphere–ocean thermal coupling on midlatitude variability. *Journal of the Atmospheric Sciences*, *55*(4), 477–493.

Battisti, D. S., & Hirst, A. C. (1989). Interannual variability in a tropical atmosphere–ocean model: Influence of the basic state, ocean geometry and nonlinearity. *Journal of the Atmospheric Sciences*, *46*(12), 1687–1712.

Bishop, S. P., Small, R. J., Bryan, F. O., & Tomas, R. A. (2017). Scale dependence of midlatitude air–sea interaction. *Journal of Climate*, *30*(20), 8207–8221.

Bitz, C. M., Shell, K. M., Gent, P. R., Bailey, D. A., Danabasoglu, G., Armour, K. C., et al. (2012). Climate sensitivity of the Community Climate System Model, version 4. *Journal of Climate*, *25*(9), 3053–3070.

Chen, C., Cane, M. A., Wittenberg, A. T., & Chen, D. (2017). ENSO in the CMIP5 simulations: Life cycles, diversity, and responses to climate change. *Journal of Climate*, *30*(2), 775–801.

Chung, E.-S., Soden, B. J., & Sohn, B.-J. (2010). Revisiting the determination of climate sensitivity from relationships between surface temperature and radiative fluxes. *Geophysical Research Letters*, *37*, L10703. https://doi.org/10.1029/2010GL043051

Cox, P. M., Huntingford, C., & Williamson, M. S. (2018). Emergent constraint on equilibrium climate sensitivity from global temperature variability. *Nature*, *553*(7688), 319–322.

Cronin, T. W., & Emanuel, K. A. (2013). The climate time scale in the approach to radiative-convective equilibrium. *Journal of Advances in Modeling Earth Systems*, *5*, 843–849. https://doi.org/10.1002/jame.20049

Dessler, A. E. (2010). A determination of the cloud feedback from climate variations over the past decade. *Science*, *330*(6010), 1523–1527.

Dessler, A. E. (2011). Cloud variations and the Earth's energy budget. *Geophysical Research Letters*, *38*, L19701. https://doi.org/10.1029/2011GL049236

Dessler, A. E. (2013). Observations of climate feedbacks over 2000–10 and comparisons to climate models. *Journal of Climate*, *26*(1), 333–342.

Donohoe, A., Armour, K. C., Pendergrass, A. G., & Battisti, D. S. (2014). Shortwave and longwave radiative contributions to global warming under increasing CO_2. *Proceedings of the National Academy of Sciences*, *111*(47), 16,700–16,705.

Forster, P. M. (2016). Inference of climate sensitivity from analysis of Earth's energy budget. *Annual Review of Earth and Planetary Sciences*, *44*, 85–106.

Forster, P. M. F., & Gregory, J. M. (2006). The climate sensitivity and its components diagnosed from Earth radiation budget data. *Journal of Climate*, *19*(1), 39–52.

Frankignoul, C. (1985). Sea surface temperature anomalies, planetary waves, and air-sea feedback in the middle latitudes. *Reviews of geophysics*, *23*(4), 357–390.

Fuller, W. A. (2009). *Measurement error models* (Vol. 305). New York: John Wiley.

Gent, P. R., Danabasoglu, G., Donner, L. J., Holland, M. M., Hunke, E. C., Jayne, S. R., et al. (2011). The Community Climate System Model version 4. *Journal of Climate*, *24*(19), 4973–4991.

Hansen, J., Ruedy, R., Sato, M., & Lo, K. (2010). Global surface temperature change. *Reviews of Geophysics*, *48*, RG4004. https://doi.org/10.1029/2010RG000345

Hansen, J. E., Sato, M., Ruedy, R., Nazarenko, L., Lacis, A., Schmidt, G. A., et al. (2005). Efficacy of climate forcings. *Journal of Geophysical Research*, *110*, D18104. https://doi.org/10.1029/2005JD005776

Hartmann, D. L. (2015). *Global physical climatology* (Vol. 103). Amsterdam: Elsevier.

Hasselmann, K. (1976). Stochastic climate models part I. Theory. *Tellus*, *28*(6), 473–485.

Jin, F.-F. (1997). An equatorial ocean recharge paradigm for ENSO. Part I: Conceptual model. *Journal of the Atmospheric Sciences*, *54*(7), 811–829.

Johnson, G. C., & Birnbaum, A. N. (2017). As El Niño builds, pacific warm pool expands, ocean gains more heat. *Geophysical Research Letters*, *44*, 438–445. https://doi.org/10.1002/2016GL071767

Kay, J. E., Deser, C., Phillips, A., Mai, A., Hannay, C., Strand, G., et al. (2015). The Community Earth System Model (CESM) large ensemble project: A community resource for studying climate change in the presence of internal climate variability. *Bulletin of the American Meteorological Society*, *96*(8), 1333–1349.

Klein, S. A., & Hall, A. (2015). Emergent constraints for cloud feedbacks. *Current Climate Change Reports*, *1*(4), 276–287.

Loeb, N. G., Wielicki, B. A., Doelling, D. R., Smith, G. L., Keyes, D. F., Kato, S., et al. (2009). Towards optimal closure of the earth's top-of-atmosphere radiation budget. *Journal of Climate*, *22*(3), 748–766.

Lutsko, N. J., & Takahashi, K. (2018). What can the internal variability of CMIP5 models tell us about their climate sensitivity? *Journal of Climate*, *31*.

Martin, T., Park, W., & Latif, M. (2013). Multi-centennial variability controlled by Southern Ocean convection in the Kiel Climate Model. *Climate Dynamics*, *40*(7–8), 2005–2022.

Meehl, G. A., Washington, W. M., Arblaster, J. M., Hu, A., Teng, H., Kay, J. E., et al. (2013). Climate change projections in CESM1 (CAM5) compared to CCSM4. *Journal of Climate*, *26*(17), 6287–6308.

Murphy, D. M., & Forster, P. M. (2010). On the accuracy of deriving climate feedback parameters from correlations between surface temperature and outgoing radiation. *Journal of Climate*, *23*(18), 4983–4988.

Proistosescu, C., & Huybers, P. J. (2017). Slow climate mode reconciles historical and model-based estimates of climate sensitivity. *Science Advances*, *3*(7), e1602821.

Richardson, M., Cowtan, K., Hawkins, E., & Stolpe, M. B. (2016). Reconciled climate response estimates from climate models and the energy budget of Earth. *Nature Climate Change*, *6*(10), 931–935.

Rose, B. E. J., Armour, K. C., Battisti, D. S., Feldl, N., & Koll, D. D. B. (2014). The dependence of transient climate sensitivity and radiative feedbacks on the spatial pattern of ocean heat uptake. *Geophysical Research Letters*, *41*, 1071–1078. https://doi.org/10.1002/2013GL058955

Spencer, R. W., & Braswell, W. D. (2010). On the diagnosis of radiative feedback in the presence of unknown radiative forcing. *Journal of Geophysical Research*, *115*, D16109. https://doi.org/10.1029/2009JD013371

Spencer, R. W., & Braswell, W. D. (2011). On the misdiagnosis of surface temperature feedbacks from variations in Earth's radiant energy balance. *Remote Sensing*, *3*(8), 1603–1613.

Stevens, B., & Schwartz, S. E. (2012). Observing and modeling Earth's energy flows. *Surveys in Geophysics*, *33*(3–4), 779–816.

Thompson, C. J., & Battisti, D. S. (2000). A linear stochastic dynamical model of ENSO. Part I: Model development. *Journal of Climate*, *13*(15), 2818–2832.

Thompson, C. J., & Battisti, D. S. (2001). A linear stochastic dynamical model of ENSO. Part II: Analysis. *Journal of Climate*, *14*(4), 445–466.

Trenberth, K. E., Fasullo, J. T., & Abraham, J. P. (2011). Issues in establishing climate sensitivity in recent studies. *Remote Sensing*, *3*(9), 2051–2056.

Trenberth, K. E., Zhang, Y., Fasullo, J. T., & Taguchi, S. (2015). Climate variability and relationships between top-of-atmosphere radiation and temperatures on Earth. *Journal of Geophysical Research: Atmospheres*, *120*, 3642–3659. https://doi.org/10.1002/2014JD022887

Tsushima, Y., & Manabe, S. (2013). Assessment of radiative feedback in climate models using satellite observations of annual flux variation. *Proceedings of the National Academy of Sciences*, *110*(19), 7568–7573.

von Storch, J.-S. (2000). Signatures of air–sea interactions in a coupled atmosphere–ocean GCM. *Journal of Climate*, *13*(19), 3361–3379.

Wang, M. C., & Uhlenbeck, G. E. (1945). On the theory of the Brownian motion II. *Reviews of Modern Physics*, *17*(2–3), 323–342.

Wielicki, B. A., Barkstrom, B. R., Harrison, E. F., Lee III, R. B., Louis Smith, G., & Cooper, J. E. (1996). Clouds and the Earth's Radiant Energy System (CERES): An Earth observing system experiment. *Bulletin of the American Meteorological Society*, *77*(5), 853–868.

Winton, M., Takahashi, K., & Held, I. M. (2010). Importance of ocean heat uptake efficacy to transient climate change. *Journal of Climate*, *23*(9), 2333–2344.

Wittenberg, A. T. (2009). Are historical records sufficient to constrain ENSO simulations? *Geophysical Research Letters*, *36*, L12702. https://doi.org/10.1029/2009GL038710

Wyrtki, K. (1985). Water displacements in the Pacific and the genesis of El Niño cycles. *Journal of Geophysical Research*, *90*(C4), 7129–7132.

Xie, S.-P., Kosaka, Y., & Okumura, Y. M. (2016). Distinct energy budgets for anthropogenic and natural changes during global warming hiatus. *Nature Geoscience*, *9*(1), 29–33.

Zhou, C., Dessler, A. E., Zelinka, M. D., Yang, P., & Wang, T. (2014). Cirrus feedback on interannual climate fluctuations. *Geophysical Research Letters*, *41*, 9166–9173. https://doi.org/10.1002/2014GL062095

Zhou, C., Zelinka, M. D., Dessler, A. E., & Klein, S. A. (2015). The relationship between interannual and long-term cloud feedbacks. *Geophysical Research Letters*, *42*, 10,463–10,469. https://doi.org/10.1002/2015GL066698